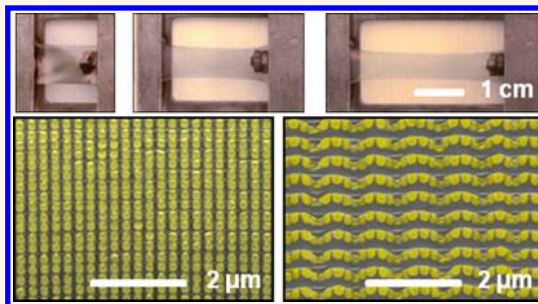


# Optics and Nonlinear Buckling Mechanics in Large-Area, Highly Stretchable Arrays of Plasmonic Nanostructures

Li Gao,<sup>†,\*,□</sup> Yihui Zhang,<sup>§,⊥,□</sup> Hui Zhang,<sup>||,□</sup> Sage Doshay,<sup>◆,□</sup> Xu Xie,<sup>†</sup> Hongying Luo,<sup>§,▽</sup> Deesha Shah,<sup>†</sup> Yan Shi,<sup>§,¶</sup> Siyi Xu,<sup>†</sup> Hui Fang,<sup>†</sup> Jonathan A. Fan,<sup>#</sup> Peter Nordlander,<sup>||,£</sup> Yonggang Huang,<sup>\*,§</sup> and John A. Rogers<sup>\*,†</sup>

<sup>†</sup>Departments of Materials Science and Engineering, Beckman Institute, and Frederick Seitz Materials Research Laboratory, University of Illinois at Urbana—Champaign, Urbana, Illinois 61801, United States, <sup>‡</sup>School of Electronic and Optical Engineering, Nanjing University of Science and Technology, Nanjing 210094, China, <sup>§</sup>Department of Mechanical Engineering and Department of Civil and Environmental Engineering, Center for Engineering and Health, and Skin Disease Research Center, Northwestern University, Evanston, Illinois 60208, United States, <sup>⊥</sup>Center for Mechanics and Materials, Tsinghua University, Beijing 100084, China, <sup>||</sup>Department of Electrical and Computer Engineering and Material Science and Nanoengineering and <sup>£</sup>Department of Physics and Astronomy, Rice University, Houston, Texas 77251, United States, <sup>#</sup>Department of Electrical Engineering and <sup>◆</sup>Department of Applied Physics, Stanford University, Stanford, California 94305, United States, <sup>▽</sup>School of Aerospace Engineering and Applied Mechanics, Tongji University, Shanghai 200092, China, and <sup>¶</sup>State Key Laboratory of Mechanics and Control of Mechanical Structures, Nanjing University of Aeronautics and Astronautics, Nanjing 210016, China. □L. Gao, Y. Zhang, H. Zhang, and S. Doshay contributed equally.

**ABSTRACT** Large-scale, dense arrays of plasmonic nanodisks on low-modulus, high-elongation elastomeric substrates represent a class of tunable optical systems, with reversible ability to shift key optical resonances over a range of nearly 600 nm at near-infrared wavelengths. At the most extreme levels of mechanical deformation (strains >100%), nonlinear buckling processes transform initially planar arrays into three-dimensional configurations, in which the nanodisks rotate out of the plane to form linear arrays with “wavy” geometries. Analytical, finite-element, and finite-difference time-domain models capture not only the physics of these buckling processes, including all of the observed modes, but also the quantitative effects of these deformations on the plasmonic responses. The results have relevance to mechanically tunable optical systems, particularly to soft optical sensors that integrate on or in the human body.



**KEYWORDS:** large-area nanodisk array · stretchable plasmonics · wide-band tunability · nanoscale buckling

Recent research demonstrates that carefully designed combinations of hard electronic nanomaterials with soft elastomers can, in optimized designs, yield high-performance integrated circuits with linear elastic responses to large strain deformations.<sup>1–6</sup> These systems are of interest partly due to their application in advanced biomedical devices that laminate on the curved, temporally dynamic surfaces of the human body, in ways that would be impossible with traditional electronics technologies.<sup>7,8</sup> Similar concepts appear to have utility in the integration of optical nanomaterials and elastomers for unusual classes of metamaterials and plasmonic structures with options in

mechanical tuning of the key properties. Recent work highlights initial examples of this type, including split ring resonators<sup>9</sup> and nanoantennas,<sup>10</sup> typically formed by electron beam lithography and then physically transferred to elastomers, or by nanostencil lithography to yield small devices (<0.01 mm<sup>2</sup>) with modest levels of elastic deformation (~10% and 21%, respectively), where linear mechanics dominate the responses. Programmable soft lithography<sup>11</sup> allows large-scale nanoparticle arrays with variable density tuned by stretching or heating using the methods of solvent-assisted nanoscale embossing. Here we report the use of advanced transfer techniques<sup>12</sup> to realize

\* Address correspondence to jrogers@illinois.edu, y-huang@northwestern.edu.

Received for review February 1, 2015 and accepted April 23, 2015.

Published online April 23, 2015  
10.1021/acsnano.5b00716

© 2015 American Chemical Society

large-scale arrays of plasmonic nanodisks on elastomer materials that can accommodate extremely high levels of strain ( $\sim 100\%$ ). The results yield nearly defect-free samples with practical sizes (several square centimeters) and the ability to tune plasmonic resonances over an exceptionally wide range, *i.e.*, nearly 600 nm. Detailed studies of the mechanics of uniaxial stretching reveal not only the expected linear variations in the spacings between nanodisks, including Poisson effects, but also nonlinear buckling that occurs above a well-defined critical strain. This buckling transforms the planar arrays into three-dimensional, noncoplanar layouts, in quantitative agreement with semianalytical theory and finite-element analysis. Experimental measurements of normal-incidence optical transmission through these structures, along with corresponding finite-element and finite-difference time-domain (FDTD) simulations, demonstrate the influence of these linear and nonlinear mechanical deformations on the optical properties.

## RESULTS

The fabrication process (Figure S1a) involves transfer printing of multilayer stacks deposited on silicon stamps that present square arrays of cylindrical posts on their surfaces (period,  $P = 300$  nm; diameter,  $D = 200$  nm; height,  $H = 300$  nm). A conformal, ultrathin layer ( $\sim 10$  nm) of a fluoropolymer minimizes the strength of adhesion to the silicon, thereby facilitating transfer. A representative stack (*i.e.*, the ink) (Figure S1b) consists of 40 nm of gold as the functional plasmonic material, with 5 nm of titanium as an adhesion promoter to a top coating of 40 nm of silicon dioxide. The disks of Au that form on the raised surfaces of the stamp have diameters of  $\sim 220$  nm ( $\sim 200$  nm from the silicon posts and an additional 20 nm from the fluoropolymer). The diameters of the SiO<sub>2</sub> disks on top are  $\sim 250$  nm, due to effects of slight angular growth during deposition.<sup>13</sup> Contact against a soft silicone substrate (thickness  $\sim 300$   $\mu\text{m}$ ) followed by mild heating promotes condensation reactions between surface  $-\text{OH}$  groups on the SiO<sub>2</sub> and the silicone, thereby creating strong bonds. Removing the stamp leaves the entire array of Au/Ti/SiO<sub>2</sub> nanodisks well adhered to the surface of the silicone, with exceptionally high yields (Figure S1c). This same procedure can be used with many other types of plasmonic metals, as shown in Figure 1a–c for the cases of gold, silver, and aluminum. The colors arise principally from plasmonic effects. Figure 1d,e show the gold sample in a tilted view and in a bent configuration to illustrate the uniformity in the color and the mechanical compliance. These systems offer extremely high levels of stretchability, where the strains (applied uniaxially) can exceed  $\sim 100\%$  before fracture, as illustrated in Figure 1f. Of particular interest here are the large-scale, 3D buckling structures that spontaneously appear above a certain critical level of uniaxial strain. Figure 1g,h present colorized (nanodisks, gold; silicone,

gray) scanning electron microscope (SEM) images (45° tilted view) that compare the arrays at zero applied strain to those at a strain of 107%. The latter reveals the 3D geometry that spontaneously results from buckling. Cartoons based on calculations of finite-element analyses (FEA) described subsequently appear in Figure 1i,j.

Figure 2a provides additional detail on this strain-induced geometry transformation. Here, SEM images (45° tilted view) reveal the changes in a given region of the sample (four rows by seven columns) for increasing levels of uniaxial strain applied along the  $y$  direction. The gaps between the nanodisks decrease in the  $x$  direction due to the Poisson effect. When the strain reaches a critical value, the spacings between the SiO<sub>2</sub> section of the nanodisks in the  $x$  direction decrease to zero. Further stretching initiates nonlinear buckling instabilities that release the strain energy. This behavior appears clearly for the case of 56% strain, where short-range ordered waves that consist of five nanodisks in a period are dominant. This structure persists but with increasing levels of out-of-plane displacement at strains of 72%, 89%, and 107%. Such behaviors can be captured using FEA simulations (Supplementary Note 1) and semianalytical methods (Supplementary Note 2) as shown in Figure 2b,c. These approximate models appear schematically in Figure S2. In the non-buckling regime, the nanodisks themselves undergo negligible deformation, as evidenced by the experimental images and the FEA results (for applied strain  $\epsilon_{\text{appl}} < 40\%$ ) in Figure 2. This response follows because the nanodisks are constructed of materials with much higher moduli than the silicone. Changes in the spacings between the nanodisks in this non-buckling regime can be captured using analytical models (Supplementary Note 2), consistent with FEA results (Figure S2c) for all cases examined. The critical strain for the onset of buckling can be solved analytically (Supplementary Note 2) by setting the nanodisk spacing along the transverse direction to zero. Beyond the critical strain, the buckled configuration is more energetically favorable compared to the nonbuckled one. In this regime, a semianalytical postbuckling model (Supplementary Note 2 and Figure S3) can be formulated by adopting buckling modes observed in experiment, similar to approaches used previously to describe buckling in thin films.<sup>4</sup> FEA and semianalytical results are consistent with experiment at all strain levels (Figure S4). Figure 2d shows the results of atomic force microscope (AFM) measurements of surface relief for a sample at 72% strain, with comparisons to FEA results in Figure 2e. The height profile along line 1 in Figure 2d indicates an average wave amplitude of  $\sim 163$  nm, which agrees well with FEA prediction ( $\sim 174$  nm) in Figure 2e. Over a 6  $\mu\text{m}$  distance, both FEA results and experiment show approximately 6 periods. The profiles along line 2 in Figure 2d and e have amplitudes of  $\sim 100$  nm, with 14.5 periods over an

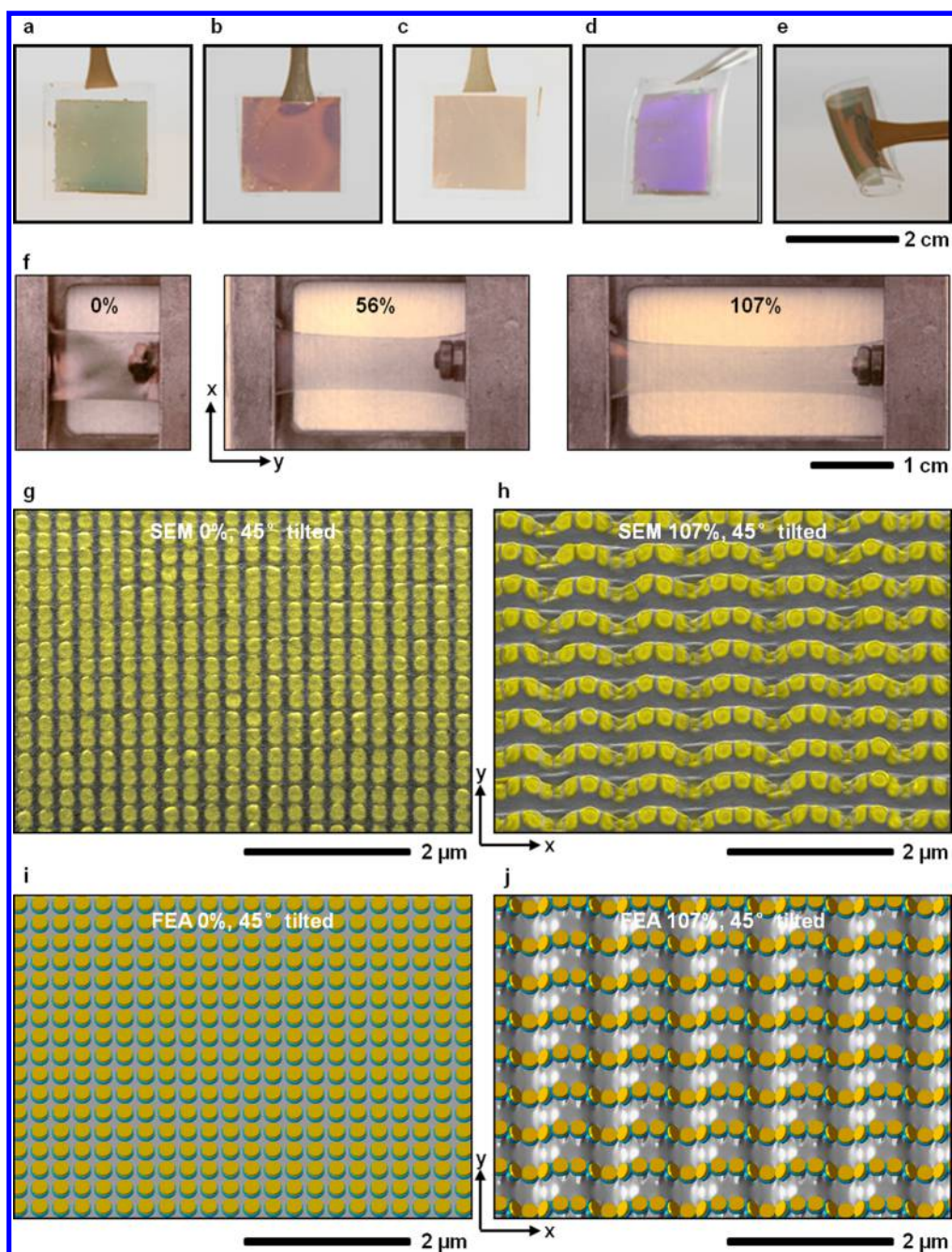
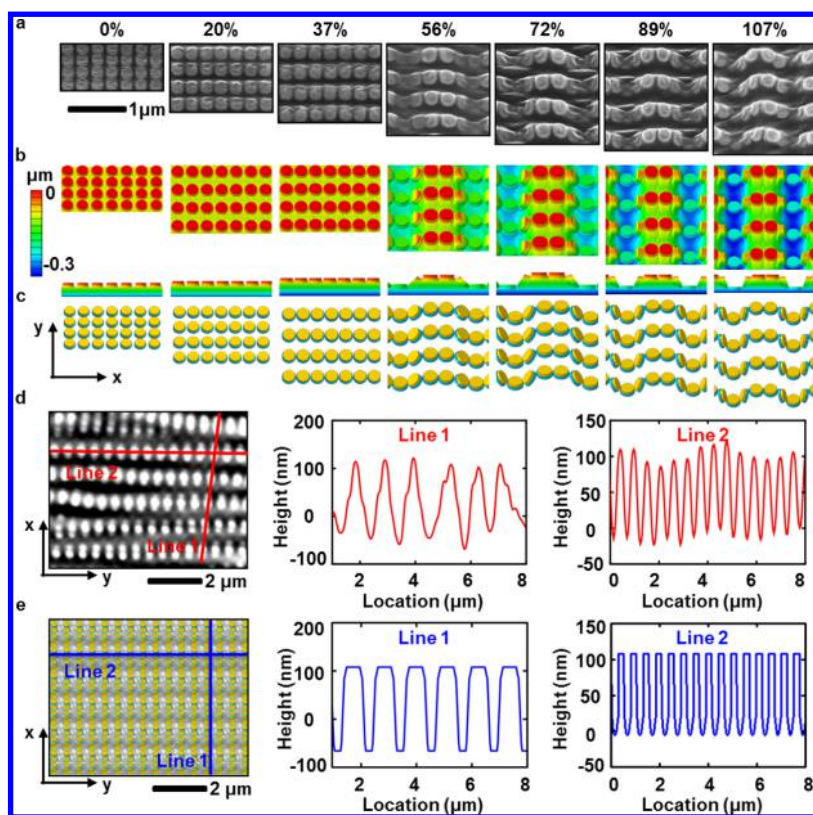


Figure 1. Arrays of plasmonic nanodisks with spacings and three-dimensional layouts that can be reversibly and continuously adjusted by mechanical stretching of a transparent elastomer support with high elastic elongation. (a) Optical image of a sample that consists of gold nanodisks. (b) Optical image of a sample that consists of silver nanodisks. (c) Optical image of a sample that consists of aluminum nanodisks. (d) Optical image of a tilted gold sample. (e) Optical image of a bent gold sample. (f) Gold sample (nanodisk period,  $P$ , of 300 nm and diameter,  $D$ , of 220 nm) under zero strain, 56% strain, and 107% strain. (g) Tilted view ( $45^\circ$ ) scanning electron microscope (SEM) image of a gold sample at zero strain. (h) Tilted view ( $45^\circ$ ) SEM image of a gold sample at 107% uniaxial strain along  $y$ . (i) FEA model of a gold sample at zero strain. (j) FEA result of a gold sample at 107% strain.

$8 \mu\text{m}$  distance, in agreement with FEA ( $\sim 100$  nm and 15 periods), where  $\sim 100$  nm corresponds to the multilayer thickness of the nanodisks ( $\sim 85$  nm). Such buckling behavior is quite different from that of continuous ribbons/films on a silicone substrate. To compare these two systems, we studied a  $\text{SiO}_2$  ribbon of the same total thickness ( $\sim 85$  nm) attached to the top of the same silicone substrate. A direct

comparison of the buckling configurations appears in Figure S5 for various levels of applied strain. The critical strain to trigger buckling in the continuous ribbons is typically much smaller than 1%,<sup>14</sup> which is much less than that ( $\sim 44\%$  in this case) for discrete nanodisks. The buckling configuration of the nanodisk system, although still in a wavy form, has characteristic wavelengths and amplitudes that



**Figure 2.** Comparison of SEM images ( $45^\circ$  tilted view) and modeling results at different levels of uniaxial strain. (a) Au nanodisk array ( $P = 300$  nm,  $D = 220$  nm) on a silicone substrate at seven different levels of uniaxial strain in the  $y$  direction. (b) Corresponding FEA results shown with  $45^\circ$  and  $90^\circ$  tilted views. The color represents the out-of-plane coordinate. (c) Corresponding semianalytical results shown with a  $45^\circ$  tilted view. (d) Surface topography measured by AFM on a sample at 72% strain. Results of line cuts along 1 and 2 appear in the frames on the right. (e) Corresponding FEA results.

are much smaller than those in the continuous films. For example, the buckling wavelength and amplitude of the nanodisk system are  $\sim 1.13$   $\mu\text{m}$  and  $\sim 0.17$   $\mu\text{m}$ , respectively, under 72% stretching (Figure S5a), as compared to  $\sim 15.78$   $\mu\text{m}$  and  $\sim 7.18$   $\mu\text{m}$ , respectively, for the continuous film system (Figure S5b).

Many buckling modes can occur and even coexist in a single, uniformly strained sample, as illustrated in the SEM image for the case of 56% strain shown in Figure 3. These results capture buckling modes with two, three, four, or five nanodisks per period, with cartoon illustrations that correspond to finite-element modeling. Empirically, these multiple modes also coexist for increased levels of strain (e.g., 72%, 89%, and 107%), with various mode transformations as a function of position across the sample and applied strain. Coexistence of these modes at a strain level of 107% is illustrated in Figure S6. Figure 4 compares different buckling modes in SEM images (Figure 4a), FEA simulations (Figure 4b), and semianalytical solutions (Figure 4c) for the case of 56% strain. The critical strain depends on a single dimensionless parameter, defined by the ratio of the period to the diameter of the nanodisks, i.e.,  $P/D$ . Analytical and FEA results appear in Figure 4d with experimental data. For strain applied along  $x$  (or  $y$ ), the red curve and circles show the critical

strains computed using semianalytical modeling and FEA, respectively. The regime above the red curve corresponds to  $P/D$  ratios that result in buckling at the corresponding strain. The green triangles and SEM images show experimental results for buckling; the purple triangles are for nonbuckling. The blue curve and circles show the critical strains for the case of stretching along a diagonal direction (i.e.,  $45^\circ$  from  $x$  or  $y$ ), which are significantly higher than those for the  $x$  (or  $y$ ) direction. The gold triangle and corresponding SEM image represent a nonbuckling condition under diagonal stretching.

Figure 5a shows large-area SEM images of a sample at 37% strain. Above the critical strain of 72%, buckling occurs across the entire area, as illustrated in Figure 5b. The buckling patterns remain constant over local regions, but over larger distances, variations occur, including (1) mode changes, e.g., from five nanodisk waves to four nanodisk patterns; (2) splitting of waves with large wavelengths into multiple (typically two) waves with smaller wavelengths, or merging of waves; (3) transformations of peaks into valleys or *vice versa*. Such behaviors depend on subtle details of the sample and cannot be easily captured by analytical modeling or FEA simulation. Figure 5c,d show tilted view ( $45^\circ$ ) SEM images along both  $x$  and  $y$  directions for the case of

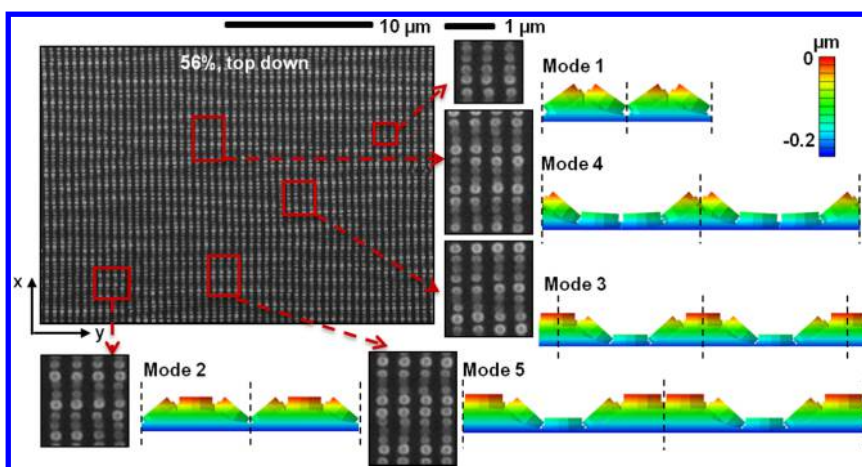


Figure 3. SEM images (top down view) and corresponding modeling results that show different buckling modes across a single sample at a strain of 56%. Buckling modes with two, three, four, and five nanodisks in a single period can be observed. The insets provide additional SEM images and corresponding cross sectional views of FEA results.

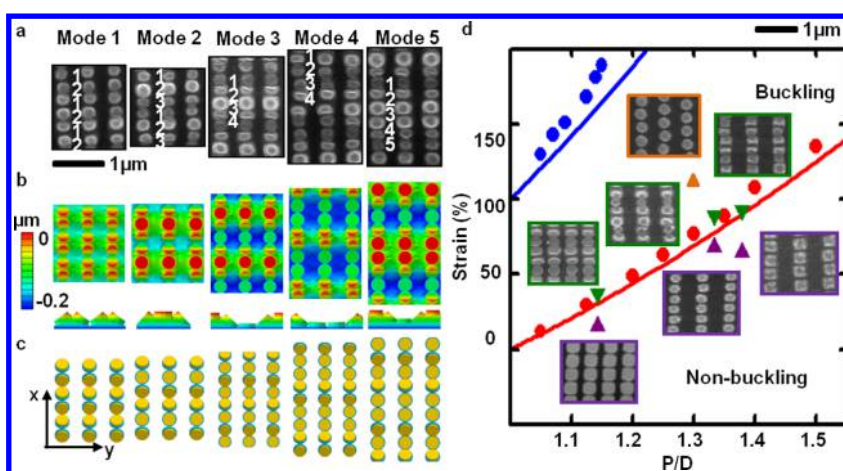


Figure 4. SEM images (top down view) and corresponding mechanical modeling results for different buckling modes. (a) SEM images of five different buckling modes that coexist at 56% uniaxial strain (along the  $y$  direction). These modes have two, three, four, or five nanodisks in a single period. (b) Top down and side views of FEA results. The color represents the out-of-plane coordinate. (c) Top down view of semianalytical results. (d) Analytical (lines) and FEA (circles) predictions of critical buckling strains under horizontal (red) and diagonal (blue) stretching, along with experimental verification (triangles) for different cases. The purple triangles and corresponding micrographs show nonbuckling conditions under horizontal stretching; green triangle and corresponding micrograph show a buckling condition under horizontal stretching; gold triangle and corresponding micrograph show a nonbuckling condition under diagonal stretching.

107% strain, with examples of each of these three types of variations. Complete sets of SEM images at different strains are in Figures S7 and S8. Figure S9 shows defect-free, large-area patterns ( $\sim 10\,000\ \mu\text{m}^2$ ) at large strain.

## DISCUSSION

Figure 6a presents transmission spectra measured for a single sample at seven different strains, normalized to a bare silicone substrate. The light source is polarized in the  $x$  direction, perpendicular to the stretching direction. Transmission spectra measured with light polarized parallel to the stretching direction (Figure S10) show comparatively smaller tunability with strain. The as-fabricated sample (nanodisks with a period of 300 nm and a diameter of 220 nm) has a resonance located at  $\sim 770$  nm. Strain induces a red shift

in this resonance, ultimately to a center wavelength of 1310 nm at 107%. The onset of buckling does not lead to a significant alteration in the nature of the strain dependence of the resonance peak, although at large strains, the depth and width of the resonance increase and decrease, respectively. Optical simulations can provide insights into the influence of various strain-induced motions of the nanodisks, which reveals that the red shifts in resonance are caused by both sheet deformation and buckling geometry. The effects of changes in spacings along the  $x$  and  $y$  directions appear in Figure S11. Increases in the spacing along the  $y$  direction and decreases in the  $x$  direction yield a uniform red shift in the resonance wavelength, similar to experiment (Figure S11b). Maintaining fixed spacing in the  $x$  direction and increasing the spacing in the  $y$

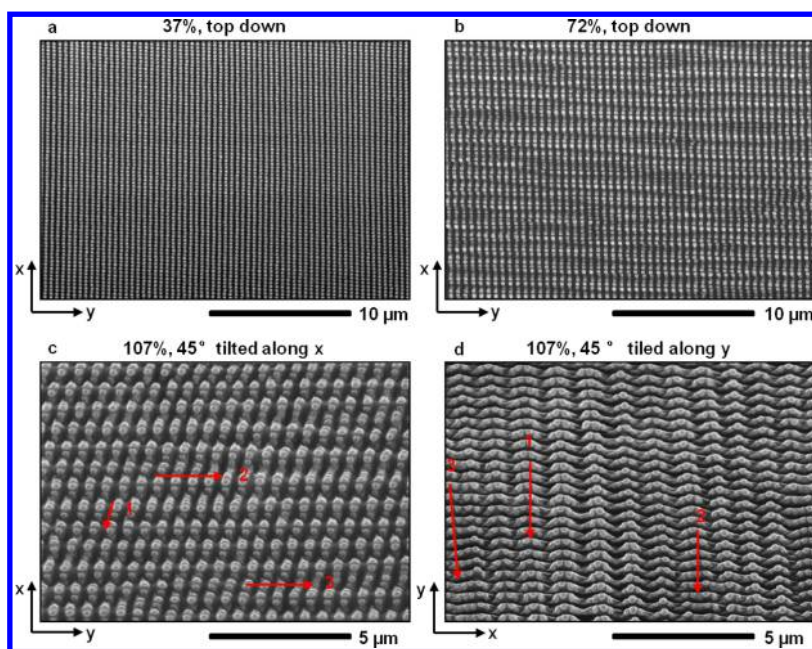


Figure 5. Large-area SEM images of samples at strains below and above the critical value for buckling. (a) Top down SEM image of a sample at a uniaxial strain of 37%. (b) Top down SEM image of the same sample at a strain of 72%. (c) SEM image (45° tilted along  $x$ ) of a sample at a uniaxial strain of 107% along the  $y$  direction. The arrows show three cases in which the buckling mode transforms gradually across a characteristic distance. (d) Similar image, collected with a 45° tilted view along  $y$ .

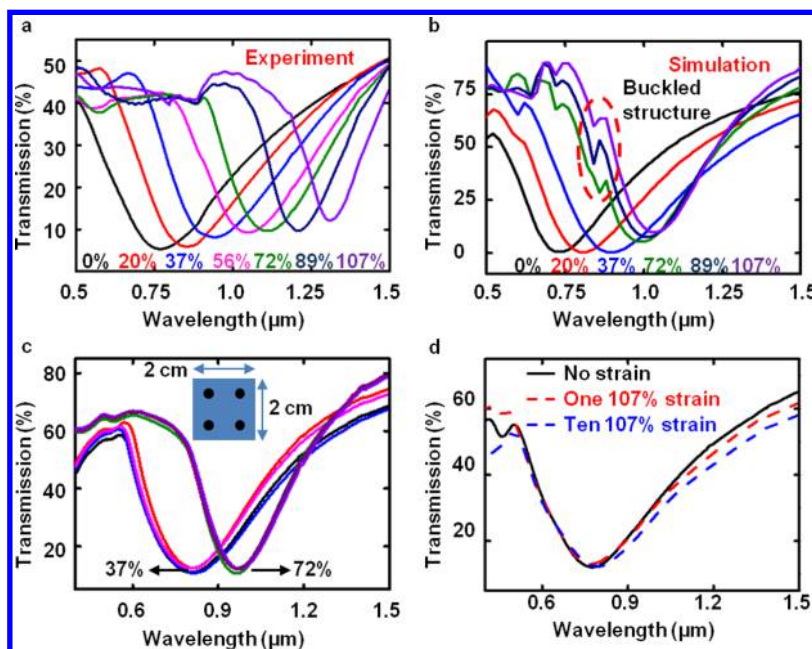


Figure 6. Measurements and modeling results for normal incidence transmission spectra obtained from arrays of plasmonic nanodisks on a transparent elastomer support, evaluated at different applied uniaxial strains. (a) Experimental results for strains between 0% and 107%. (b) Corresponding FEM simulation results. (c) Four transmission spectra, each measured at different locations across a single sample, collected at strains of 37% and 72%. (d) Transmission spectra collected after applying and releasing 107% strain 10 times.

direction only narrows the resonance (Figure S11c). On the contrary, the broadening increases at higher strain if the gap shrinks in the  $x$  direction and remains constant in the  $y$  direction (Figure S11d). Rotations of the nanodisks in the normal direction to the plane is inherent to the buckled structures, as in Figure S12.

A two-disk system examined with increasing strain provides a simpler model for understanding the effects of interdisk coupling on the continuous red shift in the resonance (Figure S12a). The origin of red-shifting can be understood by examining the electric field intensity in a plane perpendicular to the substrate and through

the center of the disks, which is plotted in Figure S12b. Each profile is shown at the wavelength specified by the minimum of the transmission dip for that strain. In the linear strain regime, as the disks approach each other, the local field intensities increase due to enhanced capacitive coupling between the disks. Physically, the edges of each disk form a capacitor, and as the gap between the disks shrinks, the capacitance increases. The result is an enhancement of local electric field and lowering of the resonant frequency of the system (*i.e.*, red-shifting). As the disks buckle and rotate relative to each other, the intensity of the hot spot continues to increase, which is indicative of even greater capacitive coupling and red shifting. The rotation of the disks yields two geometric effects that enhance coupling. First, the physical distance between the edges of the metal disks decreases, thereby increasing the capacitance. Second, as the metal disks touch and then rotate as they buckle, the effective interaction surface area between the disks increases, which also increases the capacitance. Additional studies of the effect of rotation angles for the two-disk gap mode appear in Figure S13a. Figure S13b,c compare the transmission spectra of two-disk and four-disk gap modes.

The mechanical calculations provide accurate structural information for optical simulations, by both numerical and analytical techniques. Simulation results based on waves that consist of five nanodisks per period appear in Figure 6b, where the strain varies from 0 to 107%. The results indicate that increasing levels of strain lead to systematic red shifts of the plasmon resonance peak, along with slight decreases in its depth and width. A coupling-dipole approximation method described in Figure S14 shows similar results; that is, the resonance peak red shifts with increasing strain. These overall trends are consistent with experimental results. The quantitative differences may arise, at least in part, from the various buckling modes that occur across the probed area of the sample. Accordingly, the measured transmission spectra correspond to an averaged optical response over all possible buckling modes, each of which has different

resonance and diffraction peaks. Additional simulations of the four-disk buckling geometry (mode 3) reveal resonance and diffraction peaks at longer wavelengths, up to  $\sim 1300$  nm for the highest strain levels (Figure S15). The simulations indicate that the line shapes of the transmission spectra depend on the buckling geometry at large strains. We chose buckling mode 5 for the simulations. We note the small discontinuities in the simulation results (red dashed oval in Figure 6b) arise from materials-independent diffraction effects (Figure S16). Such features depend critically on the buckling geometry and therefore do not appear clearly in the experimental results due to the spatial heterogeneity of the buckling modes. In spite of these spatial variations, the overall uniformity of the samples is excellent, as illustrated through measurement for the cases of 37% and 72% as shown in Figure 6c. Here, the transmission spectra are collected with a probing spot with a diameter of 3 mm, at locations separated by 1 cm across a sample with an area of 4 cm<sup>2</sup>. As expected, the strain-induced spectral changes are recoverable, due to the purely elastic nature of the deformations. Figure 6d compares the transmission spectra before applying strain and after releasing a strain of 107%.

## CONCLUSIONS

The unusual mechanical and optical properties of large-area, ultrastretchable, and tunable plasmonic structures like those introduced here offer strong potential in realizing different types of three-dimensional optical structures and epidermal photonic sensors with properties that can be reversibly adjusted through applied strain. With mechanical and optical modeling approaches illustrated here, complicated photonic components and structures can be designed to yield an otherwise impossible three-dimensional structures upon buckling, with uniaxial, biaxial, or radial strains. New plasmonic resonance features could be made possible, with additional real-time, wide-band tuning capabilities. Strain-induced color change and low-cost wearable plasmonic sensors represent additional opportunities.

## METHODS

**Fabrication of the Silicon Stamp.** Soft nanoimprint lithography and oxygen plasma dry etching (PlasmaTherm, chamber pressure = 15 mTorr, RIE power = 50 W, O<sub>2</sub> flow rate = 10 sccm) formed a polymer mask on a silicon wafer, following procedures described elsewhere. Etching with a Bosch process (STS Inc., chamber pressure = 94 mTorr, etch/passivation cycle time = 5 s/5 s, RIE power = 20 W/0 W, SF<sub>6</sub>/C<sub>4</sub>F<sub>8</sub> flow rate = 35 sccm/110 sccm, ICP power = 600 W) formed cylindrical features of relief on the silicon surface with a depth of  $\sim 300$  nm. Another oxygen plasma dry etching process removed the polymer mask. Exposure to C<sub>4</sub>F<sub>8</sub> in an ICP-RIE system (STS Inc., chamber pressure = 94 mTorr, passivation time = 15 s, RIE power = 0 W, C<sub>4</sub>F<sub>8</sub> flow rate = 110 sccm, ICP power = 600 W) formed an

ultrathin ( $\sim 10$  nm), uniform coating of a cross-linked fluoropolymer to facilitate release in the transfer process by reducing the degree of adhesion between the deposited multilayer stacks and the underlying silicon.

**Deposition of Multilayer Material Stacks by Electron Beam Evaporation.** The plasmonic metal films (Au, Ag, and Al), the titanium layer (adhesion promoter for the plasmonic metals), and the film of SiO<sub>2</sub> (top surface bonding layer to enable transfer printing) were deposited using an AJA International 6-pocket electron beam evaporator. Typical chamber base pressures were  $1.0 \times 10^{-8}$  Torr, and deposition rates were 0.1–0.15 nm/s.

**Transfer Printing to Elastomeric Substrates.** A low-modulus, tacky form of PDMS, created by mixing in a 35:1 ratio by weighing base and curing agent of a commercial material (Sylgard 184,

Dow Corning), served as the substrate. Exposing this material to ozone created by deep ultraviolet light (BHK Inc., grid lamp, model 88-9102-02) for 3.5 min formed reactive –OH groups on its surface. Contact with the multilayer material stacks on the raised regions of the silicon stamp initiated condensation reactions between the hydroxyl groups on the PDMS and those on the top surface layer of SiO<sub>2</sub>. Mild heating at 110 °C for 25 s led to strong bonding, such that peeling the PDMS away transferred an array of circular disks, in their entirety, from the top surface of the silicon stamp.

**Optical Measurements.** Transmission spectra were collected using a Varian Cary 5G UV–vis–NIR spectrophotometer, configured with a slit with a diameter of 3 mm and a polarizer oriented perpendicular to the stretching direction. Transmission spectra were normalized using a bare PDMS substrate.

**Conflict of Interest:** The authors declare no competing financial interest.

**Supporting Information Available:** Supplementary Notes 1–4 and Figures S1–S16 provide additional information for the results described throughout the main text. The Supporting Information is available free of charge on the ACS Publications website at DOI: 10.1021/acsnano.5b00716.

**Acknowledgment.** This work was supported by the Office of Naval Research under Grant N00014-10-1-0989.

## REFERENCES AND NOTES

- Khang, D. Y.; Jiang, H.; Huang, Y.; Rogers, J. A. A Stretchable Form of Single-Crystal Silicon for High-Performance Electronics on Rubber Substrates. *Science* **2006**, *311*, 208–212.
- Sun, Y.; Choi, W. M.; Jiang, H.; Huang, Y. Y.; Rogers, J. A. Controlled Buckling of Semiconductor Nanoribbons for Stretchable Electronics. *Nat. Nanotechnol.* **2006**, *1*, 201–207.
- Sun, Y.; Kumar, V.; Adesida, I.; Rogers, J. A. Buckled and Wavy Ribbons of GaAs for High-Performance Electronics on Elastomeric Substrates. *Adv. Mater.* **2006**, *18*, 2857–2862.
- Jiang, H.; Khang, D.-Y.; Song, J.; Sun, Y.; Huang, Y.; Rogers, J. A. Finite Deformation Mechanics in Buckled Thin Films on Compliant Supports. *Proc. Natl. Acad. Sci. U.S.A.* **2007**, *104*, 15607–15612.
- Choi, W. M.; Song, J.; Khang, D.-Y.; Jiang, H.; Huang, Y. Y.; Rogers, J. A. Biaxially Stretchable “Wavy” Silicon Nanomembranes. *Nano Lett.* **2007**, *7*, 1655–1663.
- Sun, Y.; Rogers, J. A. Structural Forms of Single Crystal Semiconductor Nanoribbons for High-Performance Stretchable Electronics. *J. Mater. Chem.* **2007**, *17*, 832–840.
- Kim, D.-H.; Lu, N.; Ma, R.; Kim, Y.-S.; Kim, R.-H.; Wang, S.; Wu, J.; Won, S. M.; Tao, H.; Islam, A.; Yu, K. J.; *et al.* Epidermal Electronics. *Science* **2011**, *333*, 838–843.
- Webb, R. C.; Bonifas, A. P.; Behnaz, A.; Zhang, Y.; Yu, K. J.; Cheng, H.; Shi, M.; Bian, Z.; Liu, Z.; Kim, Y. S.; *et al.* Ultrathin Conformal Devices for Precise and Continuous Thermal Characterization of Human Skin. *Nat. Mater.* **2013**, *12*, 938.
- Pryce, I. M.; Aydin, K.; Kelaita, Y. A.; Briggs, R. M.; Atwater, H. A. Highly Strained Compliant Optical Metamaterials with Large Frequency Tunability. *Nano Lett.* **2010**, *10*, 4222–4227.
- Aksu, S.; Huang, M.; Artar, A.; Yanik, A. A.; Selvarasah, S.; Dokmeci, M. R.; Altug, H. Flexible Plasmonics on Unconventional and Nonplanar Substrates. *Adv. Mater.* **2011**, *23*, 4422–4430.
- Lee, M. H.; Huntington, M. D.; Zhou, W.; Yang, J. C.; Odom, T. W. Programmable Soft Lithography: Solvent-Assisted Nanoscale Embossing. *Nano Lett.* **2010**, *11*, 311–315.
- Gao, L.; Shigeta, K.; Vazquez-Guardado, A.; Progler, C. J.; Bogart, G. R.; Rogers, J. A.; Chanda, D. Nanoimprinting Techniques for Large-Area Three-Dimensional Negative Index Metamaterials with Operation in the Visible and Telecom Bands. *ACS Nano* **2014**, *8*, 5535–5542.
- Gao, L.; Kim, Y.; Vazquez-Guardado, A.; Shigeta, K.; Hartanto, S.; Franklin, D.; Progler, C. J.; Bogart, G. R.; Rogers, J. A.; Chanda, D. Materials Selections and Growth Conditions for Large-Area, Multilayered, Visible Negative Index Metamaterials Formed by Nanotransfer Printing. *Adv. Opt. Mater.* **2014**, *2*, 256–261.
- Chen, X.; Hutchinson, J. W. Herringbone Buckling Patterns of Compressed Thin Films on Compliant Substrates. *J. Appl. Mech.* **2004**, *71*, 597–603.